EFDA–JET–CP(08)01/12

O. Ford, J. Svensson, A. Boboc and JET EFDA contributors

Forward Modelling of JET Polarimetry Diagnostic

“This document is intended for publication in the open literature. It is made available on the understanding that it may not be further circulated and extracts or references may not be published prior to publication of the original when applicable, or without the consent of the Publications Officer, EFDA, Culham Science Centre, Abingdon, Oxon, OX14 3DB, UK.”

“Enquiries about Copyright and reproduction should be addressed to the Publications Officer, EFDA, Culham Science Centre, Abingdon, Oxon, OX14 3DB, UK.”

Forward Modelling of JET Polarimetry Diagnostic

O. Ford[1], J. Svensson[2], A. Boboc[3] and JET EFDA contributors*

JET-EFDA, Culham Science Centre, OX14 3DB, Abingdon, UK

[1]Blackett Laboratory, Imperial College, London SW7 2BZ, UK
[2]Max-Planck-Institut für Plasmaphysik, Teilinsitut Greifswald, EURATOM-Assoziation, D-17491 Greifswald, Germany
[3]EURATOM-UKAEA Fusion Association, Culham Science Centre, OX14 3DB, Abingdon, OXON, UK
** See annex of M.L. Watkins et al, "Overview of JET Results ", (Proc. 21 st IAEA Fusion Energy Conference, Chengdu, China (2006)).*

Preprint of Paper to be submitted for publication in Proceedings of the HTPD High Temperature Plasma Diagnostic 2008, Albuquerque, New Mexico. (11th May 2008 - 15th May 2008)

ABSTRACT.

An analytical Bayesian inversion of the JET Interferometry line integrated densities into density profiles and associated uncertainty information, is demonstrated. These are used, with a detailed forward model of plasma polarimetry, to predict the rotation and ellipticity for the JET polarimeter. This includes the lateral channels, for over 45,000 time points over 1313 JET pulses. Good agreement with measured values is shown for a number of channels. For the remaining channels, the requirement of a more detailed model of the diagnostic is demonstrated. A commonly used approximation for the Cotton-Mouton effect on the lateral channels is also evaluated.

1. INTRODUCTION

The JET Interferometry/polarimetry [1] system passes 8 linearly polarised far infrared laser beams, 4 vertically and 4 laterally through the plasma in the poloidal plane (Figure 1). For each beam, the change in polarisation angle $\Delta\psi$, induced ellipticity $\in$ and the phase variation $\Delta\phi$ are measured. Provided that no rapid changes in density or loss of the signal due to refraction occur during the pulse, causing so-called 'fringe jumps', $\Delta\phi$ is routinely and reliably converted to line integrated electron density after substracting the vibration effects measured by a reference beam.

The rotation $\Delta\psi$ and ellipticity angle $\chi = \tan^{-1} \in$ are commonly related to the electron density n_e and magnetic field $\underline{B}$ by equations 1 (Faraday Effect) and 2 (Cotton-Mouton effect). Each of these is strictly only valid when the other effect is small.

$$\Delta\psi \propto \int n_e(z)\, B_{||}(z)\, dz \quad for \quad \chi \approx 0 \tag{1}$$

$$\chi \propto \int n_e(z)\, B_{\perp}^2(z)\, dz \quad for \quad \Delta\psi \approx 0 \tag{2}$$

Here, $\hat{z}$ is the beam direction and for equation 2, the polarisation angle ψ is 45^o to $\underline{B}$ in the (x, y) plane.

The beam perpendicular field $\underline{B}_{\perp}$ is predominantly the toroidal vacuum field which for the vertical channels is approximately constant since it is a stronV,function of only major radius *R*. In this case, sin χ can be used as a second measure of line integrated density[2].

For the lateral channels, where $B_{\perp} = f(z)$ (and currently the initial polarisation $\psi_0 \neq 45^o$), or where either or χ become large, a complete forward model for the polarimetry is required.

2. PLASMA POLARIMETRY MODEL

For a complete model of the polarimetry, the polarisation is represented as a stokes vector (equation 3) and its evolution is given by equation 4 [3].

$$\underline{s} = (cos2_{\chi} cos2_{\psi}, cos_{\chi} sin2_{\psi}, sin2_{\chi}) \tag{3}$$

$$\frac{d\underline{s}}{dz} = \underline{\Omega}(z) \times \underline{s} \tag{4}$$

For low temperature plasmas ($T_e \lesssim 8$keV), the vector $\underline{\Omega}$ (z) is given by equation 5, known as the cold plasma model. For higher temperatures, where electron cyclotron and relativistic effects must be included, other expressions exist [4].

$$\underline{\Omega} = \frac{w_p^2}{2cw^3\,(1 - w_c^2/w^2)} \begin{bmatrix} (e/m)^2\,(B_\chi^2 - B_y^2) \\ (e/m)^2\,2B_\chi B_y \\ 2w\,(e/m)\,B_z \end{bmatrix} \tag{5}$$

with $\hat{\underline{z}}$ the beam direction and $\hat{\underline{y}}$ the toroidal direction. $\psi = 0$ when the linearly polarised wave has $E \parallel \hat{\underline{y}}$.

To evaluate this, equation 4 is integrated along each line of sight using $\underline{B}$ (R, Z) provided by the JET equilibrium code EFIT [5] and n_e (R, Z) obtained from the interferometry.

3. INTERFEROMETRY

To obtain n_e (R, Z), a Bayesian inversion [6] is performed on the 8 measured line integrated densities D_i. The density is modelled as a 1D function of normalised poloidal flux Ψ_N. The function used is a linear interpolation of 30 nodes nej at regular intervals in $0 < \Psi_N < 1.2$. Each foward function f_i ($\underline{n}_e$) is a linear combination of these nodes $f_i(\underline{n}_e) = \Sigma_{j=1}^{N} W_{ij} n_{ej}$ where the weights W_{ij} are determined by the lines of sight for each channel and the flux surface geometry provided by EFIT. The likelihood function used is Gaussian for each channel about $f_i(\underline{n}_e)$ with $\sigma_d = 3\times10^{17}\,m^{-2}$. Through Bayes theorem, the posterior can be written in terms of this and a prior $P(\underline{n}_e)$ (equation 6).

$$P(\underline{n_e} \mid \underline{D}) \propto P(\underline{D} \mid \underline{n_e})\, P(\underline{n_e}) \tag{6}$$

The prior used is a single sided independent Gaussian in each node about 0 with $\sigma_d = 5\times10^{20}\,m^{-3}$. This is primarily to ensure the inversion is analytical but also well represents the prior knowledge that the density is unlikely to exceed JET's normal operating regime.

The full posterior can be formulated as the truncated multivariate Gaussian in ne given in equation 7, where $\underline{\underline{\sigma}}_D$ and $\underline{\underline{\sigma}}_P$ have only diagonal elements σ_d^2 and σ_p^2.

$$\begin{aligned} &P(\underline{n_e} \mid \underline{D}) \;\propto\; G(n_e;\, n_{e0}, \sigma_{n_e}) \quad \textit{for all } n_{e_j} \geq 0 \\ &\textit{with } n_{e0} = \underline{\underline{\sigma}}_{n_e}\, \underline{\underline{W}}^T\, \underline{\underline{\sigma}}_D^{-1}\, \underline{D} \\ &\underline{\underline{\sigma}}_{n_e} = [\underline{\underline{W}}^T \underline{\underline{\sigma}}_D^{-1}\, \underline{\underline{W}}^{+}\, \underline{\underline{\sigma}}_P^{-1}]^{-1} \end{aligned} \tag{7}$$

This gives the probability of any con guration of $\underline{n}_e$ given only $\underline{D}$ and the prior.
Figure 2 shows the highest probability profile and a few random samples using a) the weak prior

described above and b) a prior favouring similar n_e for neighbouring nodes. While the former appears worse, it better represents what is known about the profile from only the line integrated densities.

4. MODEL EVALUATION

At 500ms intervals in 1313 pulses, the above inversion was carried out and 300 samples drawn from the posterior. Each sampled pro le was used to predict ψ and χ for all 8 channels from the model in section II. The mean and standard deviation of these provide a representation of P (ψ/χ | $\underline{D}$, $\underline{B}$) for that time point.

Figure 3 shows the predicted (ψ_p/χ_p) and measured (ψ_m/χ_m) traces for 3 channels of a single pulse. Figure 4 shows the predicted points from all the pulses against the measured values.

Despite the large variation in the n_e profiles in figure 2a, the narrow 2σ bands show the predictions are well determined from $\underline{D}$ and $\underline{B}$ alone, with χ_p better determined than ψ_p, especially for channel 3. This is expected for the vertical channels which are well approximated by equation 2. In this case the difference (orange line) between the approximation and the full calculation is at most 7%, which is much less than the difference between either and the measurement. It is also evident that ψ_p is more sensitive to the exact n_e profile during the high density H-mode phase of this pulse (54 to 63s).

Channel 5 shows the best agreement with the measurement and where χ_p is outside the 2σ bands of χ_m, it is likely due to the random fluctions of χ_m. Neither the systematic or random uncertainties on ψ_m and χ_m are calculated here. Also not included is the uncertainty in $\underline{B}$ or the flux surface geometry. It is likely that the large disagreement with ψ_m for channel 3 is due to this, since the channel is very sensitive to the plasma core position and field, far from the magnetic sensors on which EFIT is based. For channel 6, which is not normally used due to calibration issues (see section V) shows complete disagreement with the measured χ.

Figure 4 shows the agreement between χ_p and χ_m for the 3 channels for all 1313 pulses. Again, the best agreement is in channel 5, where no systematic disagreement can be seen. Channel 3 shows good agreement but with a systematically lower prediction at very high χ. Little or no correlation can be seen in channel 6.

5. DIAGNOSTIC MODEL

Each channel has two detectors which measure orthogonal components of a beat signal created by combination of the beam with a 100Khz modulated beam. The two signals are combined electronically to produce R and R′ which ideally relate to ψ and χ by equations 8 and 9 [2], where C, Θ_0 and Φ_0 are determined by a calibration procedure in which ψ_0 is swept through a large range, before the plasma is present.

$$\begin{aligned} R &= C^{-1} \tan(\Theta + \Theta_0) \cos(\Phi + \Phi_0) \\ R' &= C^{-1} \tan(\Theta + \Theta_0) \sin(\Phi + \Phi_0) \end{aligned} \tag{8}$$

$$(\cos 2\Theta, \tan\Phi) = (\cos 2_{\chi} \cos 2_{\psi}, \tan 2_{\psi}/\sin 2_{\chi}) \quad (9)$$

In reality, the $(R, R') \Leftrightarrow (\psi, \chi)$ conversion is not this simple. K. Guenther [2] proposed an unknown optical component adding an extra phase shift. The extra unknowns are also obtained by the calibration procedure and the model is used to obtain ψ_m and χ_m from (R, R'). In some channels, e.g. 5, this works well but for others, e.g 6, it does not. Figure 5 shows the $(\psi_m(t); \chi_m(t))$ trace calculated by Guenther's model as well as a regular (R, R') grid to illustrate the mapping. Also shown is the predicted $(\psi_p(t); \chi_p(t))$ trace. It is clear from the difference between the trace during the plasma and during the calibration ($\chi = 0$), that the ellipticity information is present, just not correctly extracted. The same issue effects the other channels, to varying degrees.

Proof of the principle can be demonstrated by finding a mapping which fits (ψ_m, χ_m) to both the predictions (ψ_p, χ_p) and calibration. Figure 6 shows the (ψ_m, χ_m) trace obtained by a tted linear transformation.

While this does not provide the mapping $(R, R') \Leftrightarrow (\psi, \chi)$, a single transformation tting the whole pulse and calibration strongly supports the plasma model of section 2. Future work will concentrate on developing a model of the diagnostic including calibration, mapping and mirror vibrations to give the likelihood $P(R, R' \mid \underline{B}, \underline{n_e})$. Combined with other diagnostic likelihoods, such as the interferometry and magnetics [7], this would give a posterior that provides a consistent picture of the plasma state, including uncertainty information based on all known sources of error.

The use of the full interferometry posterior in predicting the polarimetry measurements, rather than making assumptions about the form of density profile, removes systematic effects that this might introduce. It has been shown how, despite the large apparent variation, these can correctly predict perfectly calibrated channels using the given forward model. For the less ideal cases, it has been shown that an improved diagnostic model would allow all channels to be used.

ACKNOWLEDGEMENTS

This work is being partly funded by an EPSRC CASE studentship with UKAEA Culham and has been carried out within the framework of the European Fusion Development Agreement. The views and opinions expressed herein do not necessarily reflect those of the European Commission.

REFERENCES

[1]. G. Braithwaite, N. Gottardi, G. Magyar, J. O'Rourke, J. Ryan, and D. Vron, Rev. Sci. Instrum **60**, 2825 (1989).

[2]. K. Guenther, 31st EPS Conference on Plasma Phys. London pp. P5–172 (2004).

[3]. S.E. Segre, Plasma Phys. Control. Fusion **14**, R57 (1999).

[4]. V.V. Mirnov, W.X. Ding, D.L. Brower, M. Zeeland, and T.N. Carlstrom, Phys. Plasmas **14**, 102105 (2007).

[5]. D.P. O'Brien, L.L. Lao, E. Solano, M. Garribba, T.S. Taylor, J.G. Cordey, and J.J. Ellis, Nuc. Fus. **32**, 1351 (1992).

[6]. D. Sivia, Data Analysis, A Bayesian Tutorial. (Oxford University Press, 1999), ISBN 0-19-851889-7.

[7]. J. Svensson and A. Werner, Accepted for submission to Plasma Physics and Controlled Fusion (2008).

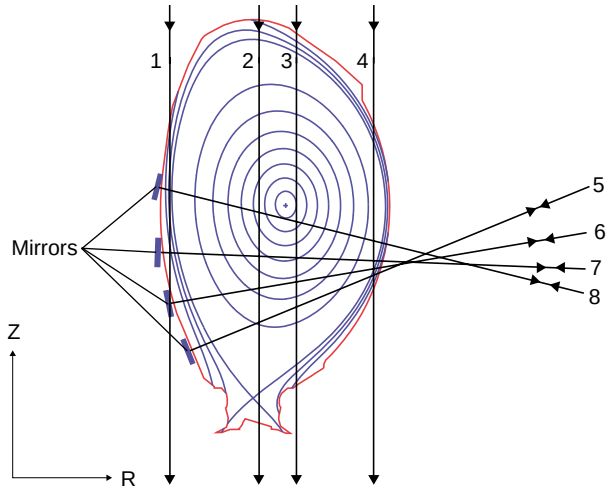

Figure 1: Lines of sight used by the 8 JET Interferometry and polarimatry channels, shown with typical flux surface geometry.

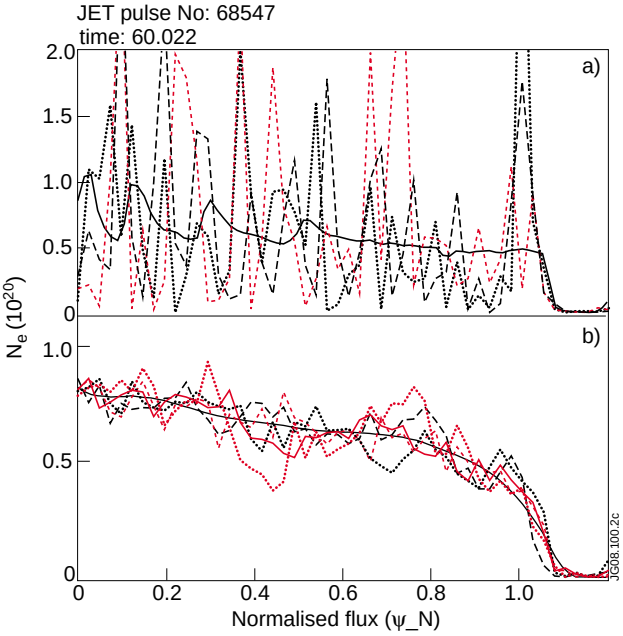

Figure2: Maximum posterior (solid) and random samples (broken) of the posterior $\underline{P}$ ($n_e|\underline{D}$) including a) only weak $n_e < 2\times10^{20}$ prior and b) a strong smoothing prior.

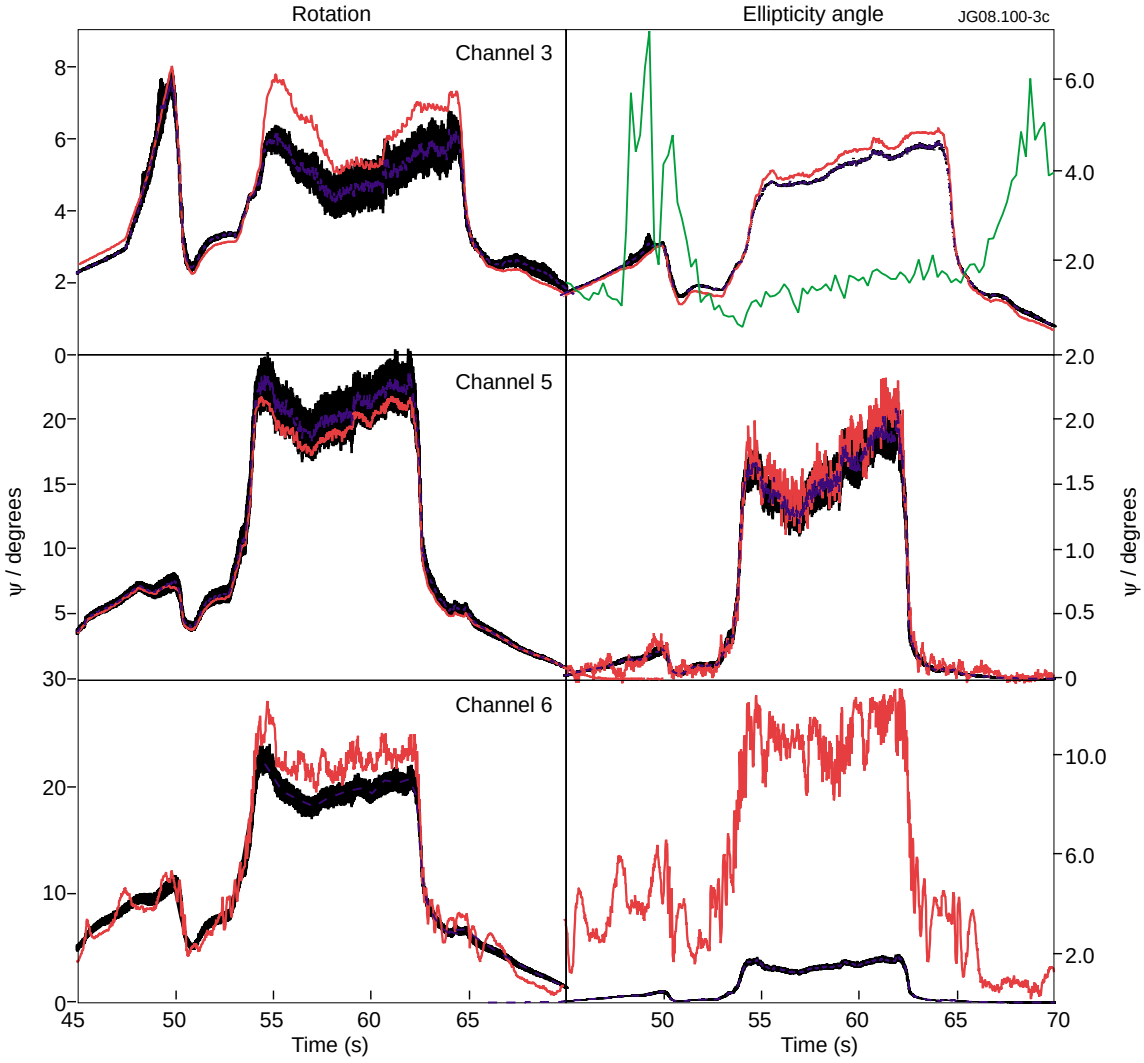

Figure 3: Predicted (blue) versus measured (red) ψ (left) and χ (right) for channels 3,5 and 6. The grey bands are ±2σ in P(y|D, B) so represent the allowable variation within uncertainty of the n_e profile. Also shown for channel 3 (green) is the difference (in percent, same scale) between the full model and equation 2. (JET Pulse No: 70545).

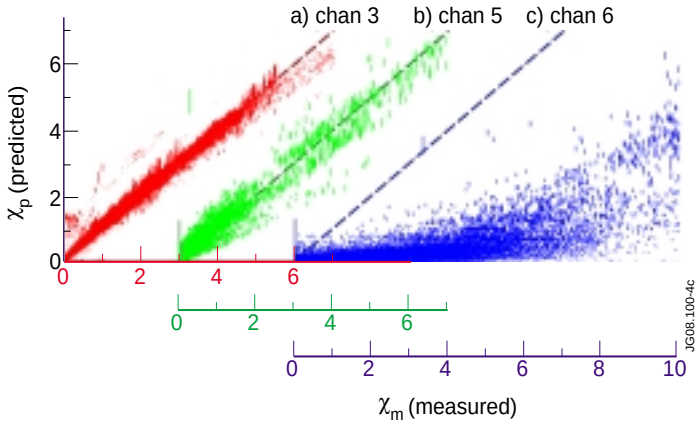

Figure 4: Predicted veraus measured (standard processing) ellipticity angle χ for 500ms samples of 1313 shots for channels a) 3, b) 5 and c) 6. Vertical lengths are ±1σ in allowable variation of n_e.

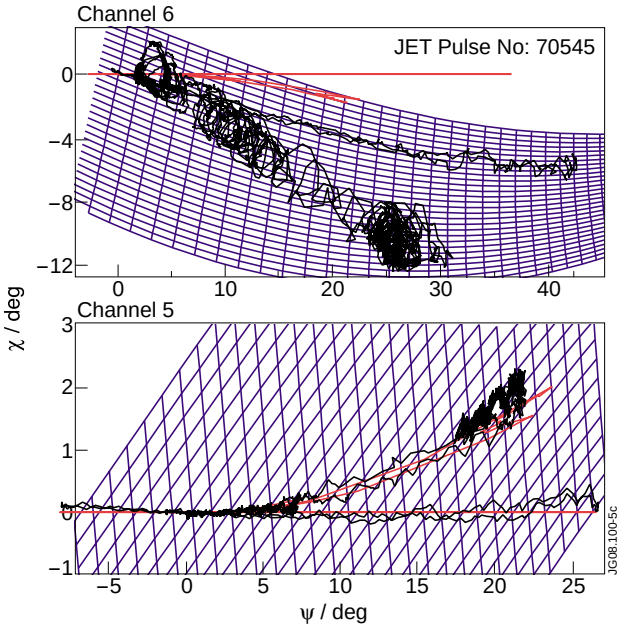

Figure 5: Mapping by Guenther's model of a regular (R, R') grid (blue) and measured data (black) to (ψ, χ). Red: predicted (ψ_p, χ_p) trace. Both traces also show calibration sweep of ψ with χ = 0.

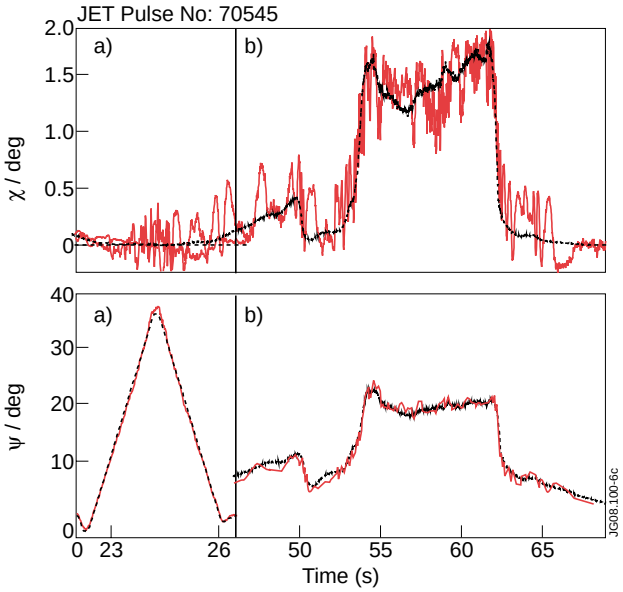

Figure 6: Predicted (blue) and remapped ψ (red) χ and during a) calibration and b) plasma for channel 6. The agreement is well within the random fluctuations.